

# ADVANCED MATERIALS

## Supporting Information

for *Adv. Mater.*, DOI: 10.1002/adma.202005920

### Strain-Mediated High Conductivity in Ultrathin Antiferromagnetic Metallic Nitrides

*Qiao Jin, Hu Cheng, Zhiwen Wang, Qinghua Zhang, Shan Lin, Manuel A. Roldan, Jiali Zhao, Jia-Ou Wang, Shuang Chen, Meng He, Chen Ge, Can Wang, Hui-Bin Lu, Haizhong Guo, Lin Gu, Xin Tong, Tao Zhu, Shanmin Wang,\* Hongxin Yang,\* Kui-juan Jin,\* and Er-Jia Guo\**

## Supplementary Materials for

**Title** Strain-mediated high conductivity in ultrathin antiferromagnetic metallic nitrides

*Qiao Jin, Hu Cheng, Zhiwen Wang, Qinghua Zhang, Shan Lin, Manuel A. Roldan, Jiali Zhao, Jia-Ou Wang, Shuang Chen, Meng He, Chen Ge, Can Wang, Hui-Bin Lu, Haizhong Guo, Lin Gu, Xin Tong, Tao Zhu, Shanmin Wang,\* Hongxin Yang,\* Kui-juan Jin,\* and Er-Jia Guo\**

Mr. Q. Jin, Dr. Q. H. Zhang, Miss. S. Lin, Dr. J. Zhao, Mr. S. Chen, Miss. M. He, Dr. C. Ge, Prof. C. Wang, Prof. H. B. Lu, Prof. T. Zhu, Prof. L. Gu, Prof. K. J. Jin, and Prof. E. J. Guo  
Beijing National Laboratory for Condensed Matter Physics and Institute of Physics, Chinese Academy of Sciences, Beijing 100190, China  
E-mail: [kjijin@iphy.ac.cn](mailto:kjijin@iphy.ac.cn) and [ejguo@iphy.ac.cn](mailto:ejguo@iphy.ac.cn)

Dr. H. Cheng and Prof. S. M. Wang  
Department of Physics, Southern University of Science and Technology, Shenzhen, Guangdong 518055, China  
E-mail: [wangsm@sustech.edu.cn](mailto:wangsm@sustech.edu.cn)

Mr. Z. Wang and Prof. H. X. Yang  
Ningbo Institute of Materials Technology & Engineering, Chinese Academy of Sciences, Ningbo 315201, China  
E-mail: [hongxin.yang@nimte.ac.cn](mailto:hongxin.yang@nimte.ac.cn)

Dr. M. A. Roldan  
Eyring Materials Center, Arizona State University, Tempe, AZ 85287, United States

Dr. J. Zhao and Prof. J. O. Wang  
Institute of High Energy Physics, Chinese Academy of Sciences, Beijing 100049, China

Mr. S. Chen and Prof. H. Z. Guo  
School of Physical Engineering, Zhengzhou University, Zhengzhou 450001, China

Prof. Xin Tong and Prof. T. Zhu  
China Spallation Neutron Source, Institute of High Energy Physics, Chinese Academy of Sciences, Beijing 10049, China

Prof. C. Wang, Prof. T. Zhu, Prof. L. Gu, Prof. K. J. Jin, and Prof. E. J. Guo  
Songshan Lake Materials Laboratory, Dongguan, Guangdong 523808, China  
and School of Physical Sciences, University of Chinese Academy of Sciences, Beijing 100190, China

Prof. E. J. Guo

Center of Materials Science and Optoelectronics Engineering, University of Chinese Academy of Sciences, Beijing 100049, China

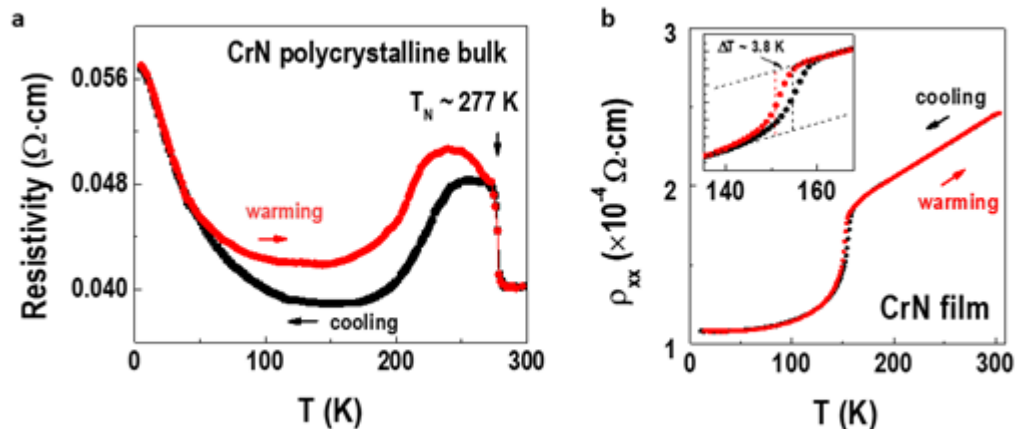


**Figure S1. Temperature dependent resistivities of a polycrystalline bulk CrN and a 200-u.c.-thick CrN film.** Previous work demonstrated that stoichiometric CrN present a phase transition at  $\sim 280$  K from a cubic ( $Fm3m$ ) paramagnet (PM) at high temperature to an orthorhombic ( $Pnma$ ) antiferromagnet (AFM) at low temperature [R1]. The structural transition was tentatively attributed to an exchange-striction effect. In (a), we observed a sharp increase of resistivity at  $\sim 277$  K in a polycrystalline bulk CrN, which was used as the ablation ceramic target. Clear resistivity loop was observed upon warming (red line) and cooling (black line). The low-temperature semiconducting behavior in the bulk CrN is attributed to the polycrystalline nature of the sample. The electron scattering from domain boundary and defects leads to the enhancement of resistivity with decreasing temperature. Similar effect had been reported in the low-quality polycrystalline CrN bulk and thin films in the past. [R2, R3] In the 200-u.c.-thick CrN films, as shown in (b), we observed a sharp decrease in the resistivity at  $\sim 150$  K. A resistivity hysteresis was determined with a temperature difference ( $\Delta T$ )  $\sim 3.8$  K with increasing/decreasing temperature. This behavior is similar to the stoichiometric bulk CrN [R3, R4]. The difference in the transition temperature is attributed to the strain effect to the electronic state and electron correlation. Below, Fig. S2 shows the misfit strain of CrN film does not fully relax when the film thickness reaches 200 u.c.

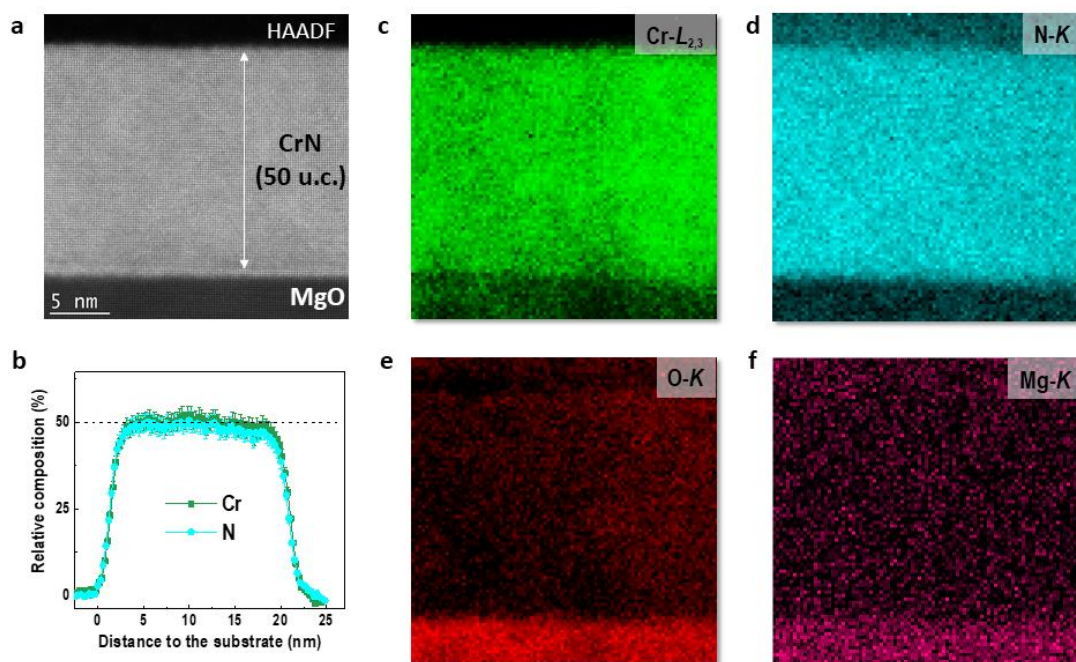


**Figure S2. Chemical composition analysis of a 50 u.c.-thick CrN film.** (a) HAADF-STEM image of CrN films with a thickness of 50 u.c. ( $\sim 20$  nm). (b) Relative composition derived from the EELS analysis along the growth direction. From the normalized EELS amplitude, the Cr : N molar ratio is close to 1, suggesting the a sufficiently low concentration of N vacancy, which is beyond the detection limit of instrument. The colored panels show the integrated intensities of (c) Cr- $L_{2,3}$ , (d) N- $K$ , (e) O- $K$ , and (f) Mg- $K$  edges, indicating the elemental distribution within the CrN layer is uniform and the CrN/MgO interface is sharp without significant chemical intermixing.

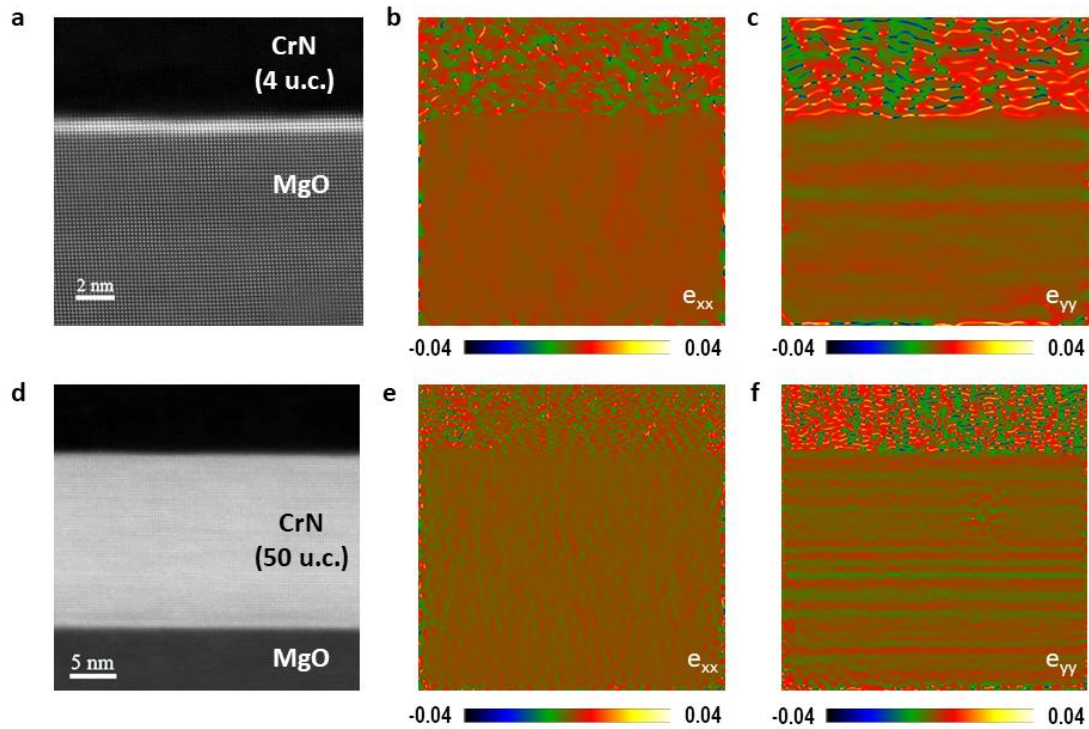


**Figure S3. Local strain analysis of two CrN films.** Low-magnification STEM images of (a) 4 u.c.- and (d) 50 u.c.-thick CrN films. We performed the geometric phase analysis (GPA) of the HAADF-STEM images. (b) [(e)] and (c) [(f)] shows the in-plane and out-of-plane strain distribution in a 4-u.c. [(50 u.c.)]-thick CrN film, respectively. The GPA results reveal the uniformed in-plane lattice constants within both CrN films and MgO substrates, consistent with the RSM results of the coherently grown CrN films with thickness below 70 u.c. For a 50-u.c.-thick CrN film, the out-of-plane lattice constant of CrN film is smaller ( $\sim 2\%$ ) than that of MgO substrates, revealing the CrN films are tensile-strained. The estimated out-of-plane lattice constant reduction from GPA is close to the results from XRD measurements, indicating a robust strain analysis from both methods. Furthermore, we do not observe a significant trend of strain relaxation and atomic structural changes in the CrN film with a thickness up to 50 u.c. Please note that the horizontal lines in (c) and (f) are caused by the extrinsic image distortion during electron beam scanning. The minor wiggle in (f) (upper right) is caused by the electron beam damage.

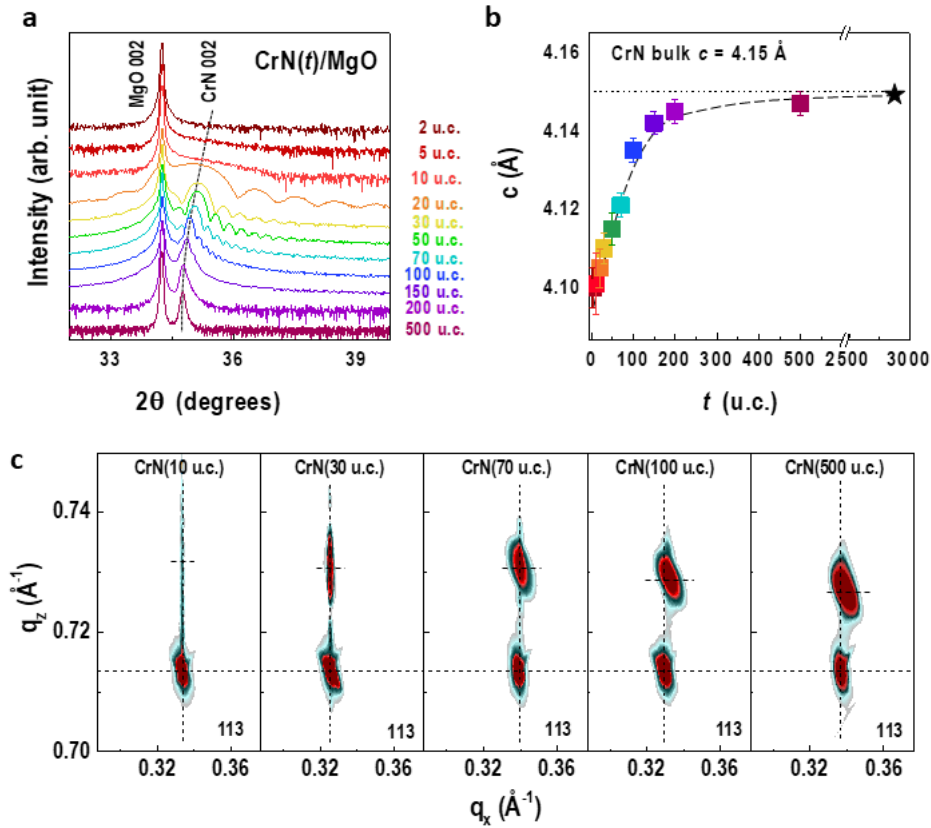


**Figure S4. Structural characterizations of CrN films with different thickness.** (a) XRD  $\theta$ - $2\theta$  scans of CrN films with thickness ranging from 2 to 500 u.c. The thickness fringes were observed in the CrN films with thickness above 10 u.c. till 150 u.c., demonstrating the high crystalline quality of all samples. The out-of-plane lattice parameters ( $c$ ) calculated from XRD  $\theta$ - $2\theta$  scans were plotted in (b). As increasing the film thickness, the  $c$  relaxes towards its bulk value  $\sim 4.15$  Å (dashed line). The black star symbol indicates the lattice parameter of the polycrystalline bulk CrN uses as the ceramic target, which is the same as previous stoichiometric samples [R4]. (c) RSM for CrN films with different film thickness around 113 peaks of film and substrate. The lattice parameters and corresponding in-plane strain are summarized in Table S1. The CrN films are coherently grown with their thickness up to 70 u.c. With film thickness further increasing, the in-plane strain starts to relax. The in-plane lattice parameter ( $a$ ) of a 500-u.c.-thick CrN film is  $4.152 \pm 0.005$  Å, while the  $c$  is  $4.147 \pm 0.005$  Å. These parameters are close to the lattice constant of bulk CrN, indicating the substrate-induced tensile strain is almost relaxed in the thickest CrN films.

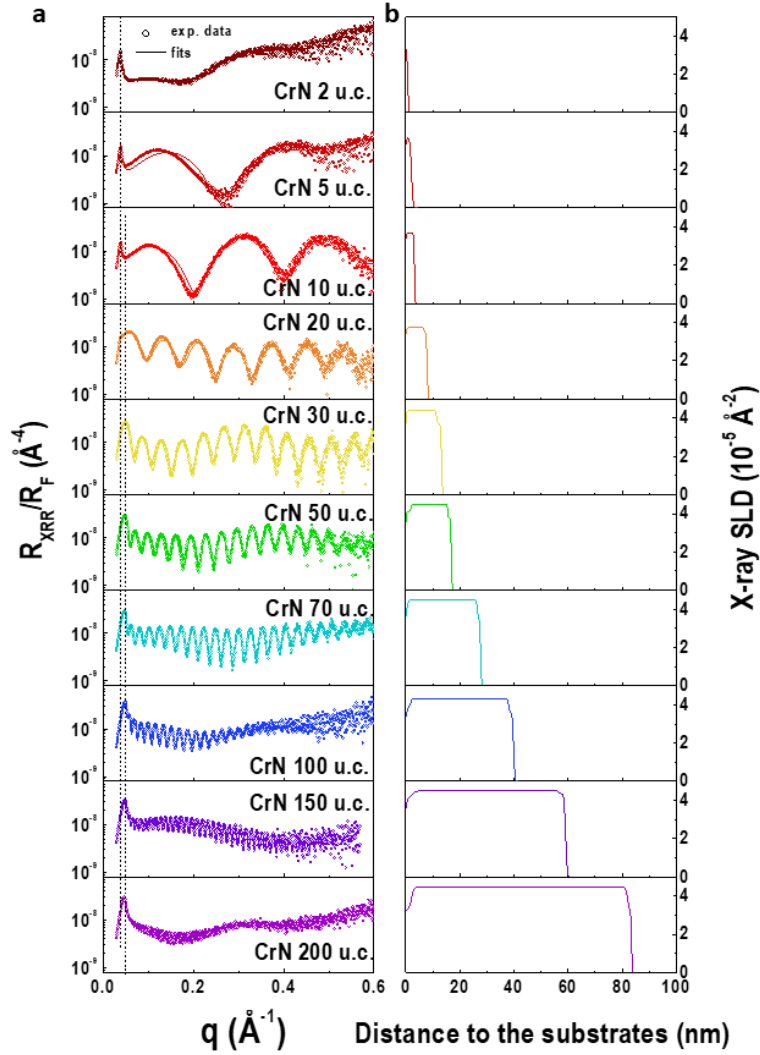


**Figure S5. X-ray reflectometry (XRR) measurements of CrN films.** XRR measurements were taken from CrN films with thickness from 2 to 200 u.c. (a) All CrN films show resolvable thickness fringes, demonstrating the smooth surface and the sharp interfaces between substrates and films. The open symbols represent the experimental data, while the solid lines are the best fit to the data using GenX software [R5]. The typical interface and surface roughness were obtained to be  $\sim (4 \pm 1) \text{\AA}$ , agreeing with the AFM measurements (not shown). The CrN film thicknesses were accurately determined from the XRR fits. We found the critical angle of XRR curves shifts from low to high  $q$  with increasing film thickness, as indicated by dashed lines. We derived the X-ray scattering length densities (SLD), which are proportional to their atomic densities, of CrN films from the XRR fits. The x-ray SLD profiles of CrN films were shown in Fig. 1(b). Apparently, for the thick CrN films, the density of CrN reaches a value close to that of stoichiometric bulk CrN ( $\sim 6.2 \text{ g/cm}^3$ ) [R6]. For the ultrathin CrN films with a thickness of just a few monolayers, the density is significantly smaller than bulk values. To find the possible mechanism, we compare a series of Cr bearing compounds of Cr,  $\text{Cr}_2\text{N}$ ,  $\text{Cr}_2\text{O}_3$ , and  $\text{CrO}_2$  with different densities of 7.15, 6.79, 5.24, 4.89  $\text{g/cm}^3$ , respectively. Therefore, the most likely reason is the nitrogen-to-oxygen substitutions at the surface of CrN. Recent work by McGahay *et al.* [R7] demonstrated that the substitutional replacement of N surface atoms with O in the epitaxial CrN layers when

expose to an O<sub>2</sub>-containing atmosphere, even at ambient conditions. However, we do not expect this effect may heavily influence our main conclusions. First of all, the O doping is fairly tiny. Only a small concentration of O impurities may increase its conductivity, while larger concentrations lead to an insulating CrO<sub>x</sub>N<sub>1-x</sub> film with a resistivity that is several orders of magnitude higher than those of our stoichiometric CrN films. Secondly, the O doping enhances the conductivity independent of the CrN film thickness. The conduction electrons provided by O doping is not fully delocalized. They also exhibit a semiconducting behavior when the thickness approaches a few monolayers in thickness. Last but not the least, the influence region is limited to just a few monolayers, as indicated by our density calculations, the upper limit of layer thickness is ~ 10 u.c., which is far below our critical thickness (~ 30 u.c.) for electronic phase transition. The exact quantity of O doping is hard to determine by either TOF-SIMS or STEM techniques because of the surface contaminations (like O<sub>2</sub>) and tiny amount of O. We believe the effect of O doping at the surface is unavoidable, however, it is negligible to our results.

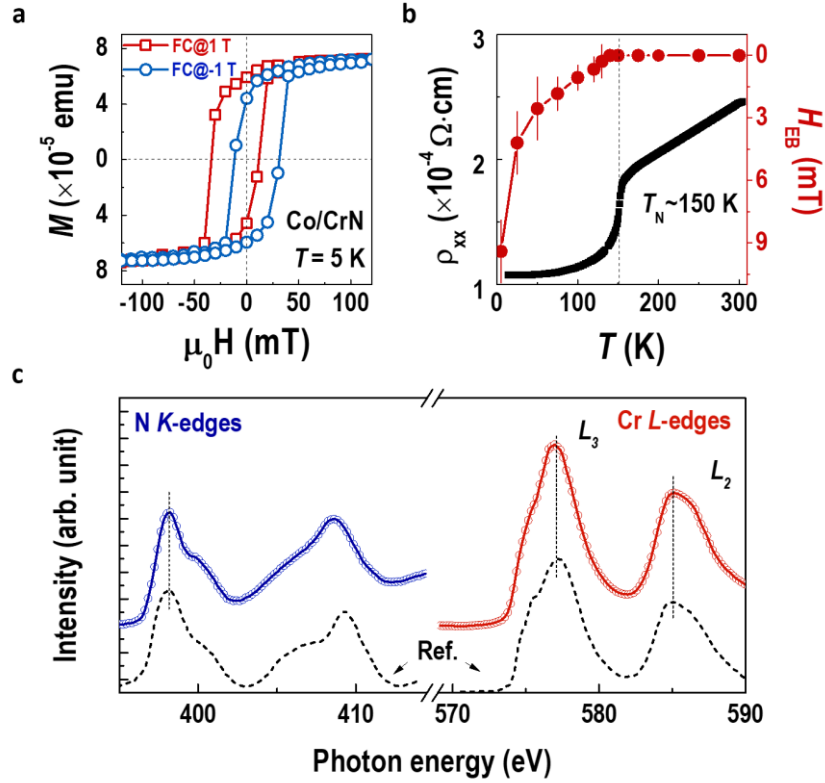


**Figure S6. Antiferromagnetic nature of CrN thin films.** (a)  $M$ - $H$  curves of a Co/CrN(200-u.c.) hybrid at 5 K. The measurements were collected after field cooling at  $\pm 1$  T from room temperature. Clear hysteresis loop shifts towards left (right) were observed after a positive (negative) field cooling from room temperature, indicating the presence of exchange bias ( $H_{EB}$ ) in the AF/ferromagnetic coupled system. Exchange bias is set in a given direction at blocking temperature ( $T_B$ ) to overcome an energy barrier to AF domain reorientation.  $H_{EB}$  and coercivity ( $H_C$ ) were determined to be  $H_{EB} = 9.4 \pm 0.5$  mT and  $H_C = 23.5 \pm 0.2$  mT at 5 K, respectively.  $H_{EB}$  reduces with increasing temperature and reaches zero value at  $\sim 150$  K, coincident with a sharp reduction of resistivity ( $\rho_{xx}$ ). (b) The temperature dependent resistivity ( $\rho_{xx}$ ) of a 200-u.c.-thick CrN film and exchange bias field ( $H_{EB}$ ) of a Co/CrN hybrid reveals a clear magnetic phase transition at  $\sim 150$  K. Besides, the  $\rho_{xx}$ - $T$  curves show clear hysteresis in the transition temperature upon heating and cooling ( $\Delta T \sim 4$  K). This behavior is in excellent agreement with that of bulk CrN, corroborating our films with high quality. (c) Elemental specific XAS of a 200-u.c.-thick CrN film for the N  $K$ -edges and Cr  $L$ -edges. The data were collected in the total electron yield (TEY) mode at room temperature. For the N  $K$ -edges, the distinct pre-peak at around 398 eV corresponds to the excitation from the N  $1s$  state to the hybridized N  $2p$ -Cr  $3d$  state. The peaks at around 577 eV and 585 eV cover the Cr  $L_3$ - and  $L_2$ -edges, respectively. Direct comparison of XAS data at both N  $K$ -edges and Cr  $L$ -edges with reference spectra from the bulk CrN indicates the valence state of Cr ions in the CrN films is  $3+$  and the N ions are strongly hybridized with Cr ions. The reference data taken from a bulk CrN were plotted in dashed lines for comparison, indicating the CrN is stoichiometric.

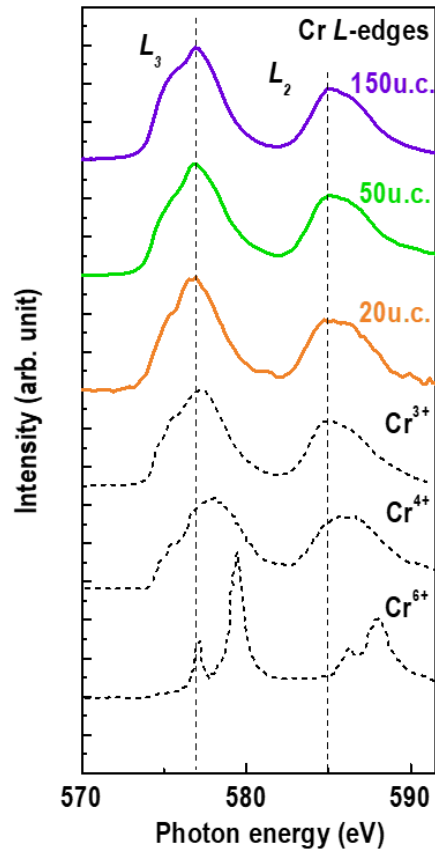


**Figure S7. XAS of CrN films for the Cr *L*-edges.** XAS for the Cr *L*-edges were measured in the CrN films with thickness of 20, 50, and 150 u.c. For comparison, the XAS of Cr<sup>3+</sup>, Cr<sup>4+</sup>, and Cr<sup>6+</sup> ions from the reference samples (bulk CrN, CrO<sub>2</sub>, and PbCrO<sub>4</sub>) were plotted in dashed lines. [R8-R10] From the line shape and XAS peak positions, the valence state of Cr in the CrN films is 3+. All films with different thickness are stoichiometric with negligible nitrogen vacancies.

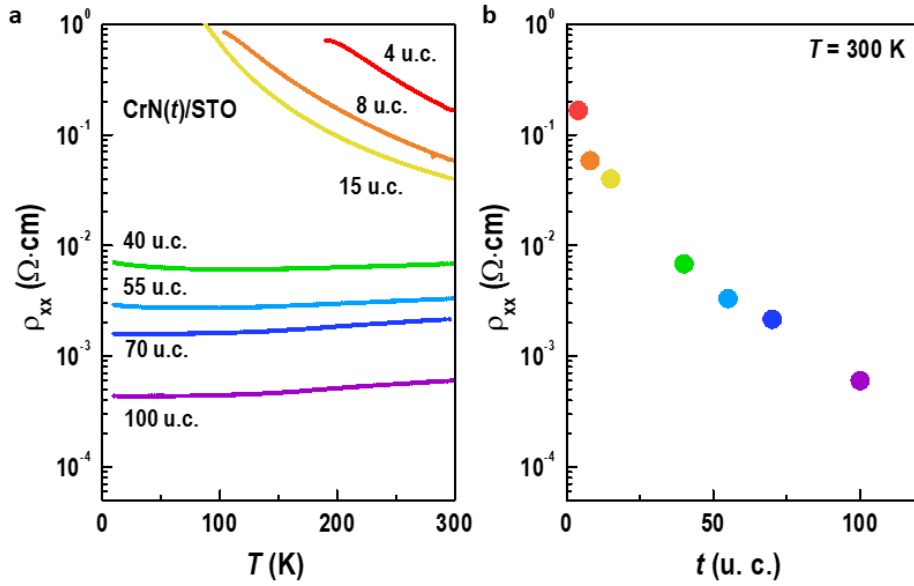


**Figure S8. Thickness dependent transport properties of CrN films grown on SrTiO<sub>3</sub> (STO) substrates.** (a) Temperature dependent  $\rho_{xx}$  of CrN films with film thickness ranging from 4 to 100 u.c. We observed a clear metal-to-insulator transition as reducing film thickness ( $t$ ). The crossover in the electronic state of CrN films happens when the film thickness below 40 u.c. We plotted the thickness dependent  $\rho_{xx}$  at room temperature. The  $\rho_{xx}$  drops significantly by three orders of magnitude with the film thickness increases from 4 to 100 u.c. The trend of  $\rho_{xx}(t)$  in CrN/STO is similar to that of  $\rho_{xx}(t)$  in CrN/MgO, indicating the universal role of controlling the electronic state transition in CrN films by epitaxial strain.

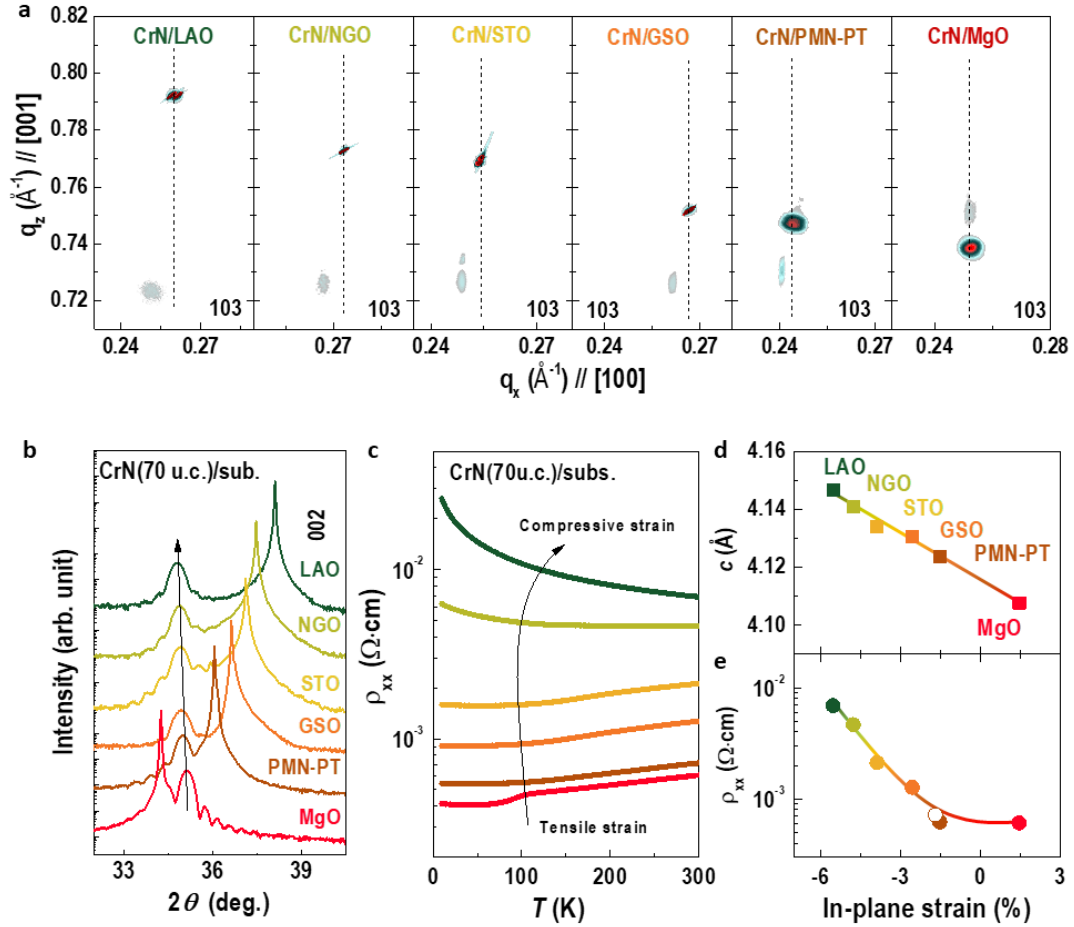


**Figure S9. Structural and electrical measurements on strained CrN films.** (a) RSMs around the 103 peaks of the substrates and CrN films, from which the in-plane strain of CrN films can be obtained. (b) XRD  $\theta$ - $2\theta$  scans of 70-u.c.-thick CrN films grown on various single crystalline substrates. XRD scans were shown over a  $2\theta$  angular range of  $32^\circ$ - $40^\circ$ . The plot shows the 002 peaks of both CrN films and substrates, confirming the epitaxial growth of the films. All CrN films show clear thickness fringes, even for the CrN film grown on the LAO substrate yielding an in-plane strain as large as  $-5.5\%$ . The XRD results demonstrate the high crystalline quality of the CrN films with different strain states. The lattice constants and in-plane strains of CrN films are summarized in Table S2. We plot the out-of-plane lattice parameters ( $c$ ) of CrN films as a function of in-plane strain in (d). We calculated the Poisson ratio of CrN using  $\nu = \delta_c / [\delta_c - (\delta_a + \delta_b)]$ , where  $\delta_a$ ,  $\delta_b$ , and  $\delta_c$  are relative strain along the [100], [010], and [001] orientations in pseudocubic lattices, respectively. The averaged  $\nu \sim 0.14 \pm 0.05$ . The large uncertainty is due to the error bars of lattice constants and possibly the formation of misfit dislocations in the highly compressive strained CrN films. We note that the Poisson ratio obtained in CrN is smaller than most of ceramics. For instance, the Poisson ratios for  $\text{SrTiO}_3$ ,  $\text{BiFeO}_3$ ,  $\text{LaScO}_3$  are  $\sim 0.23$ ,  $\sim 0.3$ , and  $\sim 0.28$ , respectively. We attribute such anomaly to the very large bulk modulus ( $\sim 361$  GPa) of CrN. This value is among the largest reported in nitrides and oxides, comparable to those of  $\text{PtN}_2$ ,  $\text{IrN}_2$ ,  $\text{MoN}$ ,  $\text{BN}$ , etc. The super hardness and stiffness of CrN makes it hard to deform elastically under the substrate-induced epitaxial strain. (c) Temperature dependent  $\rho_{xx}$  of CrN films with different strain states. Under the tensile strain, the CrN films is highly conductive with a structural transition temperature

of  $\sim 100$  K. As increasing the compressive strain, the CrN films undergo a metal-to-insulator transition. The  $\rho_{xx}$  of CrN films as a function of strain is plotted in (e). The  $\rho_{xx}(\epsilon)$  is nonlinear. In the moderate tensile and compressive strain states, the  $\rho_{xx}$  changes slightly. However, the  $\rho_{xx}$  increases dramatically when the compressive strain beyond  $-1.5\%$ , suggesting an opening of band gap when the CrN films under the large compressive strains.

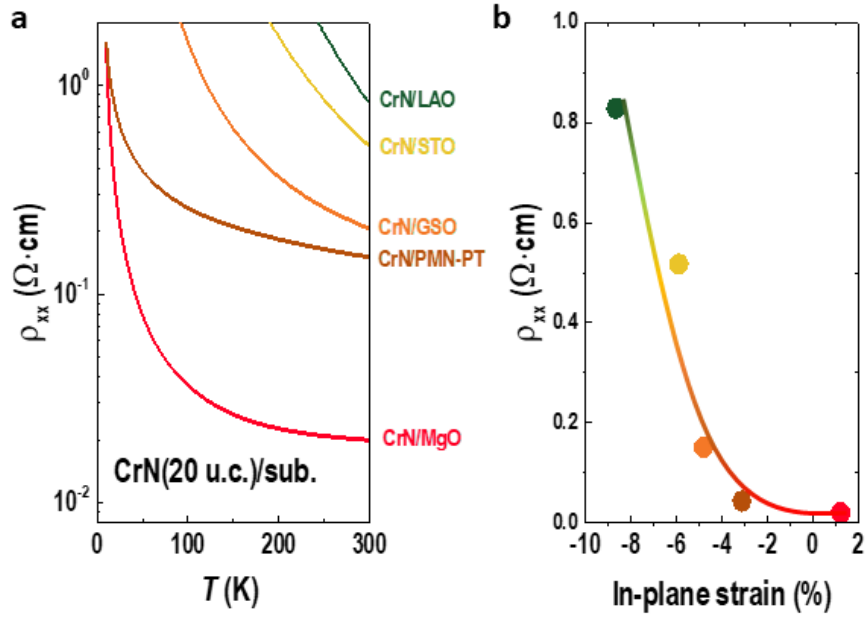


**Figure S10. Transport properties of 20 u.c.-thick CrN films under different strain states.** (a) The  $\rho_{xx}$ - $T$  curves of CrN films grown on various substrates. The thickness of CrN films is 20 u.c. ( $\sim 8$  nm), allowing the CrN films are coherently grown on the substrates. All CrN films exhibit an insulating behavior. Room-temperature  $\rho_{xx}$  of strained CrN films as a function of in-plane strain is plotted in (b). The  $\rho_{xx}(\epsilon)$  of 20 u.c.-thick CrN film is nonlinear, consistent with that of the thick CrN films.

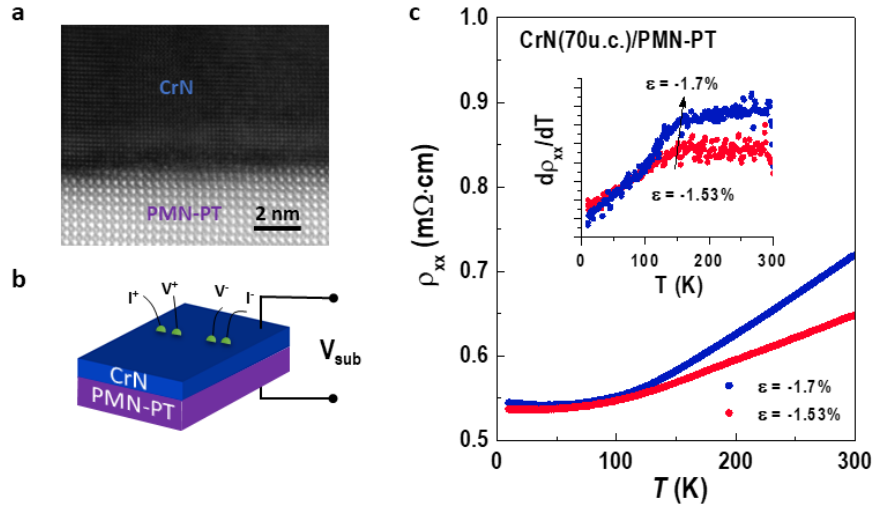


**Figure S11. Resistivity modulation by piezoelectric substrate induced strain.** (a) HAADF-STEM image of the representative interface regime between the CrN film and PMN-PT substrate. Although the surface of PMN-PT single crystal is known to be rough (the typical root mean square  $\sim 1$  nm, i. e.  $\sim 2$  u.c.) [R11], the CrN film is able to be epitaxially grown with high crystallinity. (b) Schematic measuring setup for the resistivity measurements in controlled strain states via applied bias voltage ( $V_{\text{sub}}$ ). The conductive CrN film is grounded and the  $V_{\text{sub}}$  is applied vertically across the PMN-PT substrate. The PMN-PT substrate elongates along the out-of-plane direction as a response to the applied voltage, resulting in the in-plane biaxial strain ( $\Delta\epsilon$ ) of both substrate and film. Considering the thickness of PMN-PT substrate is 3 mm, the maximum  $V_{\text{sub}}$  of 400 V induces the substrate's in-plane compression by  $\Delta\epsilon \sim -0.13 \pm 0.01$  % [R12]. (c) The  $\rho_{xx}$ - $T$  curves of a CrN film under two strain states,  $\epsilon = -1.53$  % and  $\epsilon = -1.7$  %. Inset shows the derivations of both curves, revealing a tiny change of  $T_N$  upon strain. Above  $T_N$ , the resistivity increases with increasing the compressive strain, while the resistivity barely changes at low temperatures. The room-temperature  $\rho_{xx}$  of a CrN film under two different strain states are plotted in Figure S11(e).

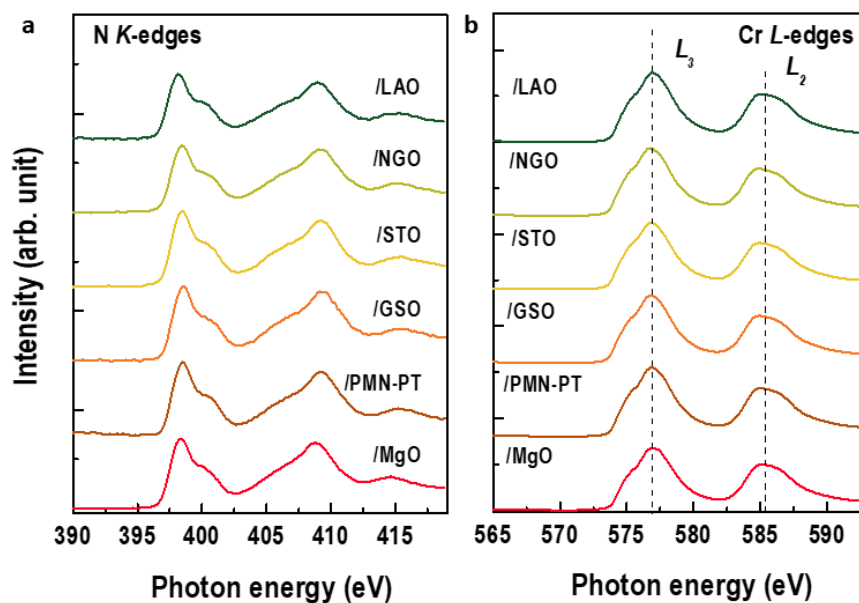


**Figure S12 XAS for (a) N  $K$ -edges and (b) Cr  $L$ -edges of CrN films grown on various substrates.** The data were collected in the total electron yield (TEY) mode at room temperature. The pre-peak position of N  $K$ -edges is around 398.2 eV for all CrN films. Similarly, the peak positions at Cr  $L_3$ - and  $L_2$ -edge are 576.8 eV and 585.4 eV, respectively, for all CrN films with different strain states. The spectroscopic results indicate the valence state of Cr keeps as 3+ and the variation of stoichiometry in strained CrN films is negligible.

**Table S1. Lattice constants of CrN films with different film thickness, which calculated from RSM measurements**

	<b>Out-of-plane lattice constant (Å)</b>	<b>In-plane lattice constant (Å)</b>	<b>In-plane strain (%)</b>
<b>CrN-10u.c.</b>	4.108	4.21	1.45
<b>CrN-30u.c.</b>	4.118	4.21	1.45
<b>CrN-70u.c.</b>	4.121	4.21	1.45
<b>CrN-100u.c.</b>	4.131	4.166	0.39
<b>CrN-200u.c.</b>	4.145	4.156	0.14
<b>CrN-500u.c.</b>	4.147	4.152	0.04

**Table S2. Lattice constants of 70-u.c.-thick CrN films grown on various single crystal substrates**

	<b>Out-of-plane lattice constant (Å)</b>	<b>In-plane lattice constant (Å)</b>	<b>In-plane strain (%)</b>
<b>CrN/LAO</b>	4.147	3.920	-5.53
<b>CrN/NGO</b>	4.141	3.951	-4.78
<b>CrN/STO</b>	4.134	3.989	-3.89
<b>CrN/GSO</b>	4.131	4.043	-2.56
<b>CrN/PMN-PT</b>	4.124	4.087	-1.52
<b>CrN/MgO</b>	4.121	4.21	1.45

## Supporting information References

- [R1]. J. D. Browne, *et al. Phys. Stat. Sol. (a)* **1**, 715 (1970).
- [R2]. D. Gall, *et al. J. Appl. Phys.* **91**, 5882 (2002).
- [R3]. C. Constantin, *et al. Appl. Phys. Lett.* **85**, 6371 (2004).
- [R4]. F. Rivadulla, *et al. Nat. Mater.* **8**, 947 (2009).
- [R5]. M. Björck and G. Andersson, *J. Appl. Cryst.*, **40**, 1174-1178 (2007).
- [R6]. M. Widenmeyer, *et al. Zeitschrift fuer Anorganische und Allgemeine Chemie (DE)* **640**, 2801-2808 (2014).
- [R7]. M. McGahay and D. Gall, *Appl. Phys. Lett.* **114**, 131602 (2019).
- [R8]. T. Ambrose and C. -L. Chien, *Phys. Rev. Lett.* **76**, 1743 (1996).
- [R9]. P. A. Bhohe, *et al. Phys. Rev. Lett.* **104**, 236404 (2010).
- [R10]. M. Wu, *et al. J. Phys. Chem. C* **118**, 23274-23278 (2014).
- [R11]. R. C. Devries, *et al. J. Am. Ceram. Soc.* **51**, 72–75 (1968).
- [R12]. E. J. Guo, *et al. Adv. Mater.* **27**, 1615-1618 (2015).